

1 **Stress drop variation of deep-focus earthquakes based**
2 **on empirical Green's functions**

3 **Meichen Liu¹, Yihe Huang¹, and Jeroen Ritsema¹**

4 ¹Department of Earth and Environmental Sciences, University of Michigan, Ann Arbor, MI 48109, USA

5 **Key Points:**

- 6 • Empirical Green's function analysis of the stress drops of deep-focus earthquakes
7 • One standard deviation range are 3.5–369.8 MPa for P waves and 8.2–328.9 MPa
8 for S waves
9 • The median stress drops suggest that fault shear stress is an order of magnitude
10 higher in the mantle than in the crust

Abstract

We analyze source characteristics of global, deep-focus (>350 km) earthquakes with moment magnitudes (M_w) larger than 6.0–8.2 using teleseismic P-wave and S-wave spectra and an empirical Green’s functions approach. We estimate the corner frequency assuming Brune’s source model and calculate stress drops assuming a circular crack model. Based on P-wave and S-wave spectra, the one-standard deviation ranges are 3.5–369.8 MPa and 8.2–328.9 MPa, respectively. Based on the P-wave analysis, the median of our stress-drop estimates is about a factor of ten higher than the median stress drop of shallow earthquakes with the same magnitude estimated by Allmann and Shearer (2009). This suggests that, on average, the shear stress of deep faults in the mantle transition zone is an order of magnitude higher than the shear stress of faults in the crust. The wide range of stress drops implies coexistence of multiple physical mechanisms.

Plain Language Summary

The change of shear stress (i.e., stress drop) during an earthquake is thought to be larger for deeper earthquakes than shallow earthquakes because of higher overburden pressure. However, the observational evidence for stress drop dependence on depth is still inconclusive. We estimate stress drops of earthquakes deeper than 400 km from recorded ground motion spectra. We find that the median stress drop of deep earthquakes is about one order of magnitude higher than the stress drop of shallow (<50 km) earthquakes. This implies that the shear stress of deep faults is moderately higher than of faults in the crust. The wide range of our stress drop estimates suggests that various mechanisms producing deep earthquakes coexist.

1 Introduction

High temperatures and superimposed stresses in excess of 1000 MPa should inhibit brittle failure at depths larger than 50 km. However, approximately 25% of earthquakes occur at these large depths (Frohlich, 1989) and they have nearly double-couple mechanisms. This suggests that deep earthquakes involve shear faulting on a planar surface similar to crustal earthquakes.

Previous studies have proposed two physical mechanisms of deep-focus (> 350 km) earthquakes as shear failures: (1) metastable phase transformation (e.g., Kirby, 1987; H. Green & Burnley, 1989; H. W. Green & Houston, 1995) and (2) shear-induced melting (e.g., Aki, 1972; Kanamori et al., 1998; Karato et al., 2001). In the first mechanism, small lenticular cracks nucleate as a result of the volume decrease during the olivine-to-spinel phase transformation and form macroscopic faults. In the second mechanism, frictional melts on pre-existing faults lubricate the fault plane, reduce dynamic shear strength, and facilitate earthquake rupture. Once triggered, a shear instability evolves into a cascading failure (Chen & Wen, 2015), which may propagate at a super-shear rupture velocity (Zhan et al., 2015).

Previous studies of deep-focus earthquakes produced inconsistent results. For example, Poli and Prieto (2016) determined that the radiation efficiencies of intermediate-depth (30–350 km) and deep-focus earthquakes are different. Persh and Houston (2004) related distinct changes of aftershock productivity at depths of 300 km and 550 km to different metastable phase transformations. Both studies suggest a change of the rupture mechanism with depth. In contrast, Campus and Das (2000) did not observe an obvious difference in the spectral properties and the source time functions of intermediate-depth and deep-focus events. The global invariance of strain drops with depth based on the analysis of source time functions (Vallée, 2013) indicates that one single mechanism could be responsible for all earthquakes.

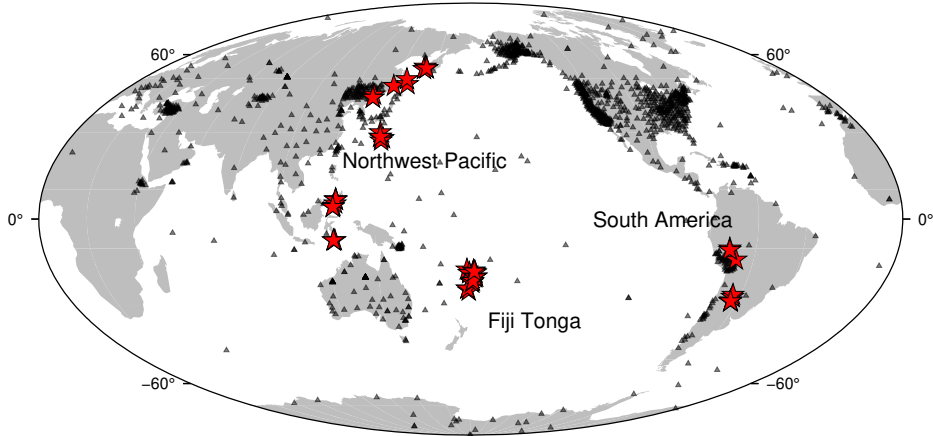


Figure 1. Global distribution of master events (stars; see also Table 1) and stations (triangles) used in this study

In this paper we evaluate whether stress drops of shallow and deep-focus earthquakes are significantly different. Stress drop is the difference between shear stresses along the fault before and after an earthquake. It is a fundamental parameter for understanding the physics of the rupture process (Kanamori & Brodsky, 2004). If the shear-failure processes are similar, deep-focus earthquakes should exhibit higher stress drops than shallow earthquakes due to larger fault shear stresses.

Early studies by Aki (1972) and (Kanamori & Anderson, 1975) suggested stress drops of deep earthquakes are an order of magnitude larger than the range of 1–10 MPa of crustal earthquakes. However, recent analyses of larger data sets indicate that stress drops of crustal earthquakes can vary significantly and that stress drops of shallow and deep earthquakes are similar. For example, the stress drops of 95% of global crustal earthquakes studied by Allmann and Shearer (2009) are between 0.22 and 66 MPa. Poli and Prieto (2014) and Poli and Prieto (2016) found the stress drops of 95% of earthquakes at depths of 400–700 km are 3.6–49.2 MPa.

To measure stress drops of deep-focus earthquakes (Figure 1), we analyze teleseismic P-wave and S-wave spectra using the spectral ratio approach based on empirical Green’s functions (eGfs) (Huang et al., 2016). We compare our stress drops of deep-focus earthquakes to those of shallow earthquakes estimated by Allmann and Shearer (2009), the only published stress drop study for global shallow earthquakes based on eGfs.

2 Methods

2.1 Corner Frequency and Stress Drop Estimates

The spectrum of a teleseismic P wave or S wave is $u(f) = S(f)P(f)R(f)$, where the factors S , P , and R are the source, path and receiver-side contributions, respectively. We can determine the ratio of the source spectra $S_M(f)$ and $S_{eGf}(f)$ by dividing the P-wave or S-wave spectra u_M for a large earthquake (i.e., the master event) by the spectra u_{eGf} for a smaller nearby earthquake (i.e., the eGf) recorded at the same station (Aki, 1967; Mueller, 1985; Frankel & Wennerberg, 1989; Imanishi & Ellsworth, 2006; Abercrombie, 2015). For the Brune source model (Brune, 1970) $S(f, f_c) = M_0/(1+(f/f_c)^2)$, where M_0 is the seismic moment and f_c is the corner frequency, $S_M(f)/S_{eGf}(f)$ has a sigmoidal shape with a high plateau at low frequencies determined by the ratio of the

89 seismic moments and a spectral fall-off between the corner frequencies of the master event
 90 and the eGf. From here on, we denote the corner frequencies of the master event and
 91 the and the eGf as f_M and f_{eGf} .

92 Abercrombie (2015) recommended to select eGfs that are located within one-source
 93 dimension of the master event in order to cancel out $P(f)$ and $R(f)$. We therefore choose
 94 eGfs at hypocentral distances within 100, 300, and 500 km from master events with mo-
 95 ment magnitudes in the range of 6–7, 7–8, and 8–9 (only two events), respectively. Us-
 96 ing a distance threshold of 300 km for the two Mw8 events does not significantly change
 97 our stress drop estimates. We require the eGfs to have magnitudes that are at least 0.5
 98 lower to ensure that f_M and f_{eGf} are distinguishable. We allow eGfs to have different
 99 focal mechanisms because the source-radiation effects are small when spectra are aver-
 100 aged from stations over a wide range of source azimuths (Calderoni et al., 2015; Ross &
 101 Ben-Zion, 2016).

102 The source radius r of a master earthquake is related to f_c by $r = kv/f_c$, where
 103 v is the S-wave velocity varying with depth. We assume a circular shear crack model,
 104 so the stress drop $\Delta\tau$ is related to r as $\Delta\tau = 7M_0/16r^3$ (Eshelby, 1957). Houston (2015)
 105 has shown that the majority of deep-focus earthquakes have rupture velocities that range
 106 between 50% and 90% of the shear-wave velocity. Here we assume that the rupture ve-
 107 locity is 90% of the shear-wave velocity, and choose $k_P = 0.32$ for P wave and $k_S =$
 108 0.21 for S wave following Madariaga (1976) to facilitate the comparison with Allmann
 109 and Shearer (2009). If we assume that the rupture velocity is 50% of the shear-wave ve-
 110 locity, $\Delta\tau$ estimated from P-wave and S-wave spectra would increase by a factor of \sim
 111 2.5 and ~ 1.7 , respectively, based on estimates of k_P and k_S by Sato and Hirasawa (1973)
 112 and Kaneko and Shearer (2014).

113 2.2 P-wave and S-wave Spectral Ratio Analysis

114 We analyze P-wave and S-wave spectra using vertical-component and transverse-
 115 component waveforms recorded at epicentral distances smaller than 85 degrees. We ap-
 116 ply the multi-window method (Imanishi & Ellsworth, 2006; Huang et al., 2016) to stack
 117 spectra for five windows that are each 40 s long and overlap by 20 s. The first window
 118 begins 5 s before the theoretical (i.e., PREM; Dziewonski & Anderson, 1981) arrival time.
 119 The windows include coda waves with important source information (Aki & Chouet, 1975).
 120 We find that stacked spectra for window lengths from to 120 seconds are not significantly
 121 different.

122 We use data with a signal-to-noise ratio (SNR) higher than 2 in each of the frequency
 123 bands 0.025–0.1 Hz, 0.1–0.4 Hz, 0.4–0.9 Hz, and 0.9–2.0 Hz. The SNR is defined as the
 124 ratio of the average amplitudes in the 40-s long window before the arrival times. We av-
 125 erage the spectral ratios from at least three stations. The corner frequency f_M may be
 126 underestimated when it is within a factor of 1.5 (Ruhl et al., 2017) to 3.0 (Abercrombie,
 127 2015) of the maximum signal frequency. It is difficult to resolve f_M if the low-frequency
 128 plateau is not distinguishable from the high-frequency spectral fall-off but we can esti-
 129 mate f_M reliably if it has a value between 0.05 and 0.67 Hz. Due to the limited band-
 130 width of our data, f_{eGf} is poorly resolved for most eGfs.

131 After resampling the P-wave and S-wave spectra evenly in the log domain, we es-
 132 timate f_M of the master event and its uncertainty by fitting the average spectral ratio
 133 to the theoretical curve in the 0.025–2.0 Hz frequency range using two approaches. The
 134 first approach is based on a grid search. We compute the least-squares misfit between
 135 the stacked and the theoretical spectral ratios (assuming the Brune model) as a func-
 136 tion of f_M and f_{eGf} for a fixed moment ratio determined by the spectral ratio at the low-
 137 est frequencies. In the second approach, we estimate f_M using the Trust-Region-Reflective
 138 least squares algorithm by (Branch et al., 1999). We bootstrap the residuals between the
 139 observed and the best-fit spectral ratios at each frequency and create a synthetic spec-

140 tral ratio by adding the bootstrapping residuals to the best-fit spectral ratios. We re-
 141 peat this process 1,000 times to obtain a Gaussian distribution of f_M values for 1,000
 142 synthetic spectral ratios. The 95% confidence interval is similar to the range of resolved
 143 values along the 1.01 misfit contour (defining the minimum misfit to be 1). We retain
 144 an estimate of f_M only when its distribution has a two-standard deviation smaller than
 145 0.05 in the log domain, which is within 0.89–1.12 times the best-fit corner frequency. We
 146 likely underestimate the uncertainties in the estimate of the corner frequency because
 147 we have not considered the effects of imperfect cancellation of propagation path and site
 148 effects in our analysis.

149 Figure 2 illustrates our analysis for the 2013 Sea of Okhotsk earthquake (Event 5
 150 in Table S1). Figure 2a shows station-averaged P-wave spectral ratios for three eGfs (2009/12/01,
 151 Mw6.3; 2013/10/01, Mw6.7; 2013/05/24, Mw6.7). The estimates of f_M range from 0.075
 152 to 0.15 Hz. Three panels in Figure 2b show that the spectral of the three eGfs can be
 153 matched by theoretical ratios within a misfit of 1.01 when estimates of f_M of Event 5
 154 vary between 0.11–0.13 Hz for eGf 1, 0.074–0.08 Hz for eGf 2, and 0.14–0.16 Hz for eGf
 155 3. The bootstrapping results in Figure 2c indicate that f_M is 0.12 Hz, 0.08 Hz, and 0.15
 156 Hz for eGfs 1, 2, and 3, respectively. In Table S1, we report that Event 5 has a corner
 157 frequency $f_M = 0.11 \pm 0.01$ Hz based on this analysis.

158 3 Estimates of Corner Frequencies and Stress Drop

159 Our analysis is based on global waveform data of earthquakes from 2000 to 2018
 160 listed in the ANSS Comprehensive Earthquake Catalog with focal depths larger than 400
 161 km and moment magnitudes higher than 5.5. Using 2,860 P-wave recordings of 28 earth-
 162 quakes and 2,296 S-wave recordings of 29 earthquakes, we measure 116 and 95 corner
 163 frequencies from analyses of P-wave and S-wave spectra that meet the quality control
 164 criteria. We show observed and modeled spectral ratios in Figure S1 and document source
 165 parameters in Table S1.

166 Figures 3a and 3b show estimates of f_M from the analysis of P waves and S waves,
 167 respectively. The P-wave corner frequencies vary from 0.05 to 0.67 Hz, which is the same
 168 as the resolvable frequency range, whereas the S-wave corner frequencies vary from 0.06
 169 to 0.26 Hz. In Supplementary Figure S2 we show that the estimates of f_M are similar
 170 for the Boatwright model (Boatwright, 1980), which predicts a steeper decrease of the
 171 source spectra at frequencies higher than f_M . f_M varies by a factor of 6 (for S waves)
 172 to 10 (for P waves) but a dependence on magnitude is not obvious. For example, f_M for
 173 events 41 and 53 (see Supplementary Figure S1) are similar although the event magni-
 174 tudes are different by about 1. The magnitudes of events 36, 42, and 53 are between 7.6
 175 and 7.9 but estimates of f_M for these events differ by a factor of 10.

176 Since f_M does not depend on magnitude, the stress drop $\Delta\tau$ increases with mag-
 177 nitude (Figure 3c, 3d). Poli and Prieto (2016) also observe an increase of $\Delta\tau$ with mo-
 178 ment from for 415 earthquakes deeper than 100 km. However, the stress-drop increase
 179 may be due to the narrow range of resolvable corner frequencies in our dataset. The one-
 180 standard-deviation ranges of $\Delta\tau$ for P waves and S waves are 3.5–369.8 MPa and 8.2–
 181 328.9 MPa, respectively. The median values of 50.0 and 51.0 MPa are higher than the
 182 estimate of 13.4 MPa from Poli and Prieto (2016). We do not observe a dependence of
 183 stress drop on event depth and focal mechanism (Supplementary Figure S3 and S4 (Shearer
 184 et al., 2006)). However, the earthquakes with the highest (event 42) and lowest (event
 185 54) P-wave corner frequencies and stress drops have double-couple components smaller
 186 than 40%. Since the Brune source model is based on shear failure of a planar fault, the
 187 corner frequencies of non-double-couple events may be poorly resolved.

188 In Figure 4, we compare our P-wave estimates of f_M and $\Delta\tau$ to the estimates from
 189 Allmann and Shearer (2009) who analyzed shallow (<50 km) earthquakes using teleseis-

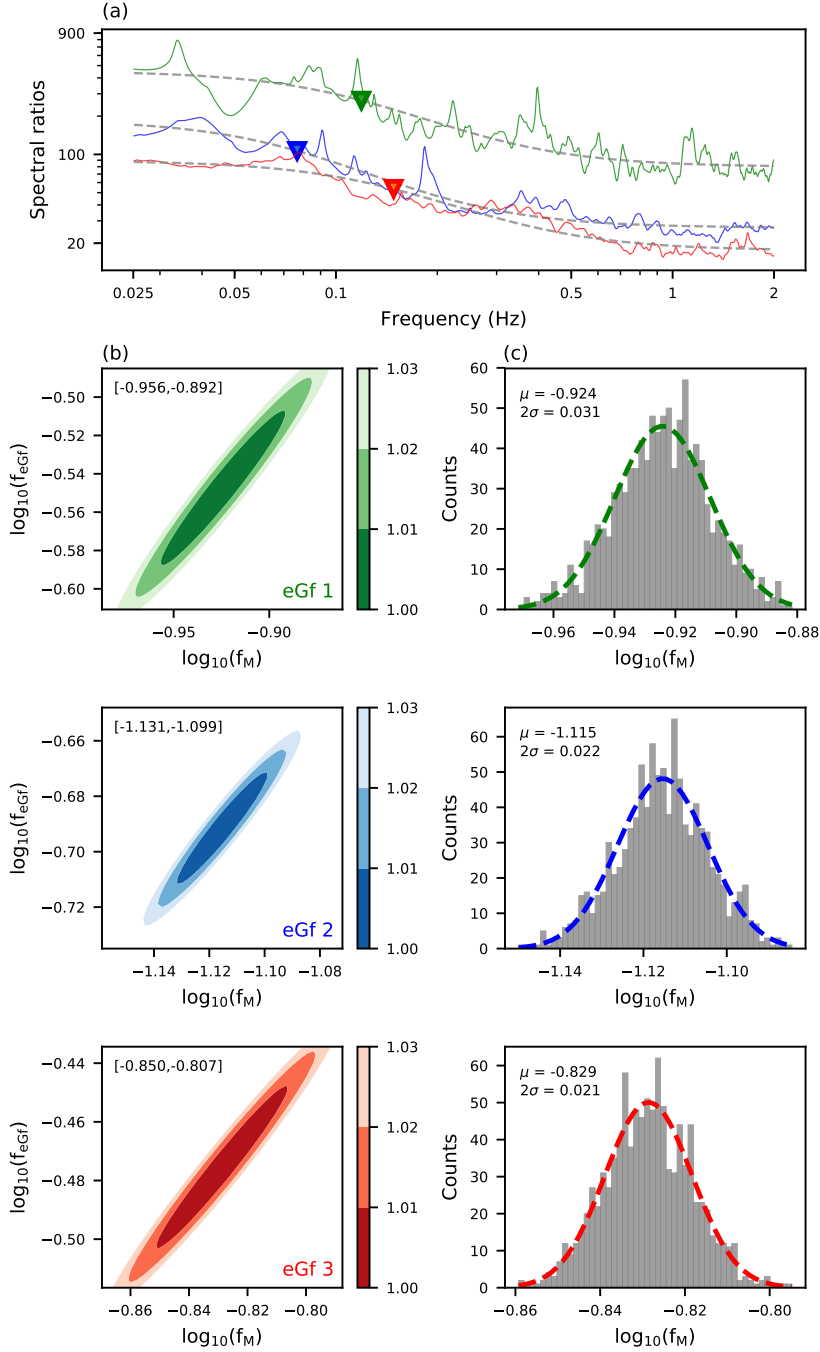


Figure 2. (a) Estimates of the S-wave spectral ratios (green, blue, and red solid lines) and corner frequencies (green, blue, and red triangles) of Event 5 (May 24, 2013; Sea of Okhotsk) based on three eGfs. The best-fit ratios are shown with dashed lines. (b) Contours of the misfit (scaled to minimum misfit) as a function of the corner frequencies of the master event (x-axis, $\log_{10}(f_M)$) and the eGf (y-axis, $\log_{10}(f_{eGf})$) for the same three eGfs as in (a). Values in the upper left of each panel indicates the variation of $\log_{10}(f_M)$ for a misfit of 1.01. (c) Histograms of the estimated $\log_{10}(f_M)$ based on bootstrapping analysis. Dashed curves are best-fitting Gaussians. Means (μ) and two-standard deviations (2σ) are indicated on the upper left of each panel. Note that spectral ratios and results of grid search and bootstrapping for the same eGf are depicted in the same color

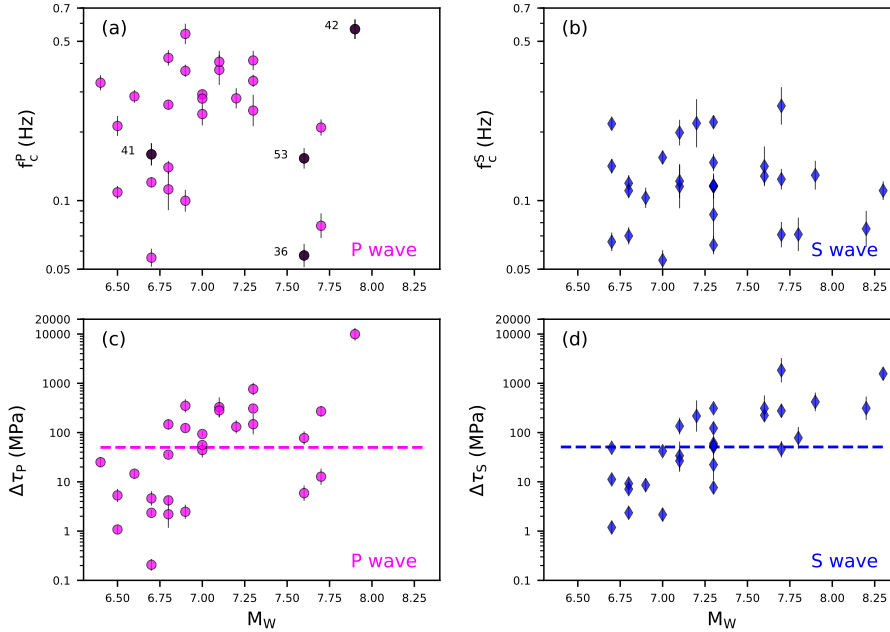


Figure 3. Corner frequencies (a and b) and stress drops (c and d) of master events as a function of moment magnitudes estimated from P-wave (a and c) and S-wave spectra using Brune’s source model. Vertical lines indicate 2σ uncertainties determined by bootstrapping analysis. (a) Numbers to the left of four data points are the associated event numbers in Table 1. Dashed lines in (c) and (d) indicate medians of P-wave (50.0 MPa) and S-wave (51.0 MPa) stress drops estimates.

190 mic P waves and globally averaged empirical Green’s functions. The highest value for
 191 $\Delta\tau$ in Allmann and Shearer (2009) is 1000 MPa. Assuming a Gaussian distribution, 95%
 192 of their stress drops are between 0.22 and 66 MPa and have a median value of 4.0 MPa.
 193 Thus, Figure 4 suggests that the median stress drop of the shallow earthquakes is 12.5
 194 times smaller than the median stress drop of deep-focus earthquakes in the same mag-
 195 nitude range.

196 4 Discussion

197 Our studies indicates that the stress drop of deep-focus earthquakes is higher than
 198 the stress drop of crustal earthquakes. This suggests that the mantle transition zone can
 199 accommodate shear faulting with higher stress drops. However, the difference in stress
 200 drop of shallow and deep-focus earthquakes may partly originate from the applied ap-
 201 proaches. Shearer et al. (2019) compared the spectral ratio approach used in this study
 202 with the global eGf fitting approach used by Allmann and Shearer (2009). They found
 203 that, for the Brune source model, corner frequencies of a cluster of Landers aftershocks
 204 estimated using the spectral ratio approach are systematically higher than estimates us-
 205 ing the global eGf fitting approach. However, it cannot explain the one-order-of-magnitude
 206 difference in the stress drops of shallow and deep-focus earthquakes shown in Figure 4.
 207 Moreover, assuming the Boatwright source model, the estimated corner frequencies have
 208 less scatter and there is better agreement between the two approaches.

209 The one-standard-deviation range of 3.5–369.8 MPa of the estimated stress drop
 210 (using P waves) implies that different physical mechanisms underlie deep-focus earth-

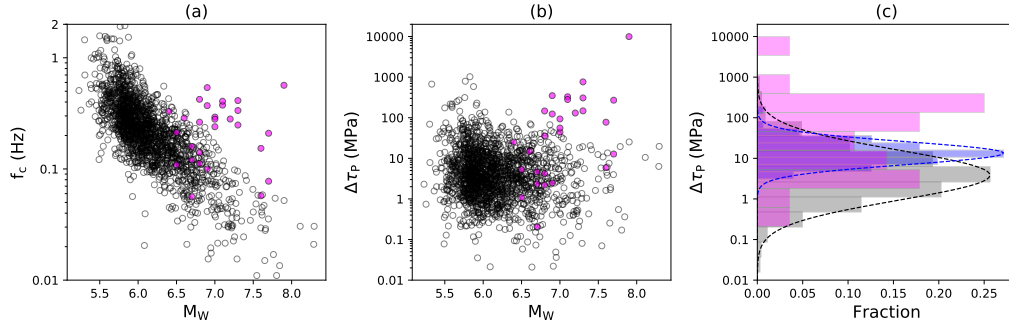


Figure 4. (a) Corner frequencies and (b) stress drops of shallow earthquakes (white circles) by (Allmann & Shearer, 2009) and estimates for deep-focus earthquakes in this study (magenta circles). (c) Histograms of the stress drop distributions corresponding to data in (a) and (b). The blue histogram shows the stress-drop distribution of deep-focus earthquakes determined by Poli and Prieto (2016). Dashed lines are Gaussian contour fitting to histograms. The median stress drops of magenta, blue, and gray histograms are 50.0 MPa, 13.4 MPa, and 4.0 MPa.

211 quake faulting. Shear-induced melting can accommodate shear failure with higher stress
 212 drops than phase transformation due to the large reduction of fault friction. The stress
 213 drop of the 1994 Mw8.3 Bolivia earthquake is estimated to be higher than 100 MPa (e.g.
 214 Antolik et al., 1996; Kikuchi & Kanamori, 1994) and faulting may have caused shear-
 215 induced melting (Kanamori et al., 1998; Zhan et al., 2014). In contrast, the 2013 Mw8.3
 216 Sea of Okhotsk earthquake has a much smaller stress drop of 12–15 MPa (Ye et al., 2013)
 217 and may have been triggered by phase transformation (Zhan et al., 2014). Deep focus
 218 earthquakes may also involve a combination of shear melting and phase transformation
 219 (Meng et al., 2014; Zhan, 2017; Fan et al., 2019).

220 In our analysis, the source radius r can be much smaller than the dimension of the
 221 rupture plane estimated from finite-fault inversions or back-projection studies because
 222 our estimate of the corner frequency is primarily sensitive to the area of the fault plane
 223 with highest slip. For example, we estimate that $r = 9.4$ km for the May 24, 2013 Sea
 224 of Okhotsk earthquake (Event 5 in Table 1), whereas Ye et al. (2013) determined by kine-
 225 matic slip inversion that fault plane was 180 km long and 60 km wide. Similarly, we es-
 226 timate $r = 16.2$ km for the August 19, 2018 Fiji earthquake (Event 19 in Table 1), which
 227 implies a much smaller rupture area than 80 km by 100 km determined by Fan et al. (2019)
 228 from a back-projection analysis. In contrast, our estimate and the estimate by Ruiz et
 229 al. (2017) of the source radius and stress drop of the November 24, 2015 Peru earthquake
 230 (Event 53 in Table 1) are similar. It is important to study variations of stress drop us-
 231 ing consistent approaches.

232 Our results suggest that the fault shear stress in the mantle transition zone is one
 233 order of magnitude higher than in the crust. This is significantly smaller than the two
 234 orders of magnitude difference of pressure in the crust and mantle (100s MPa versus 10s
 235 GPa). High-pressure and high-temperature experiments (e.g. Paola et al., 2015; H. Green
 236 et al., 2015) indicate that ground-boundary sliding may weaken faults and facilitate deep-
 237 focus earthquakes generation if accompanied by phase transformation. This is consis-
 238 tent with the weak dependence of sliding resistance on confining stress along faults trig-
 239 gered by olivine-spinel phase transformation in Me_2GeO_4 observed by Tingle et al. (1993).
 240 In addition, the effective friction coefficient is smaller than 0.01 inferred by H. Green et
 241 al. (2015), suggesting that shear failure process can occur at stresses significantly smaller
 242 than the value to overcome static friction through laboratory experiments under high-

243 pressure conditions. Goto et al. (1987) estimate that the principal stress due to olivine-
 244 spinel phase transition is larger than 500 MPa for an equilibrium phase transition and
 245 larger than 2 GPa for a nonequilibrium transition. Yoshioka et al. (1997) have shown
 246 that the buoyancy forces caused by the density differences associated with the phase trans-
 247 formation can produce a maximum shear stress of 23 MPa along the metastable wedge
 248 using physical properties determined from high P-T experiments and 2-D finite element
 249 models, which may enable shear process under the condition of low principle stress. Fur-
 250 thermore, the amplitudes of stresses estimated from buoyancy forces (Bina, 1997; Yosh-
 251 ioka et al., 1997) can be comparable to the stresses level on crustal faults.

252 5 Conclusion

253 We measure the corner frequencies of global deep-focus earthquakes using the spec-
 254 tral ratio analysis based on teleseismic P-wave and S-wave spectra and a Brune source
 255 model. We find the one standard deviation ranges of P-wave and S-wave stress-drop es-
 256 timates are 3.5–369.8 MPa and 8.2–328.9 MPa, respectively. The median of the P-wave
 257 and S-wave stress-drop estimates are 50.0 MPa and 51.0 MPa, respectively. These me-
 258 dians are about one order of magnitude higher than the median stress drop of global shal-
 259 low earthquakes estimated by Allmann and Shearer (2009). The large variation of stress
 260 drops implies that both phase transformation and shear heating processes play impor-
 261 tant roles in the rupture processes of deep-focus earthquakes. Despite the two-orders-
 262 of-magnitude difference in the pressure in the mantle transition zone and crust, the com-
 263 parison of median stress drops of shallow and deep-focus earthquakes suggests that the
 264 fault shear stress in the mantle is one order of magnitude higher than shear stresses in
 265 the crust.

266 Acknowledgments

267 This research was supported by NSF grant EAR 1565511 to JR and University of Michi-
 268 gan support to YH. The IRIS Data Services and the IRIS Data Management Center pro-
 269 vide provide the Global Seismographic Network (GSN) waveforms and related metadata
 270 used in this study. We thank Priero Poli for providing his catalog of stress drops of deep-
 271 focus earthquakes. We thank the editor (Gaven Hayes) and anonymous reviewers for help-
 272 ful comments. Corner frequency and stress drop estimates are archived in the Deep Blue
 273 Data repository at <https://doi.org/10.7302/sp05-y333>. They are also archived in Table
 274 S1 in the Supporting Information.

275 References

- 276 Abercrombie, R. E. (2015). Investigating uncertainties in empirical Green’s function
 277 analysis of earthquake source parameters. *Journal of Geophysical Research:*
 278 *Solid Earth*, *120*(6), 4263–4277.
- 279 Aki, K. (1967). Scaling law of seismic spectrum. *Journal of geophysical research*,
 280 *72*(4), 1217–1231.
- 281 Aki, K. (1972). Earthquake mechanism. *Tectonophysics*, *13*(1-4), 423–446.
- 282 Aki, K., & Chouet, B. (1975). Origin of coda waves: source, attenuation, and scat-
 283 tering effects. *Journal of geophysical research*, *80*(23), 3322–3342.
- 284 Allmann, B. P., & Shearer, P. M. (2009). Global variations of stress drop for mod-
 285 erate to large earthquakes. *Journal of Geophysical Research: Solid Earth*,
 286 *114*(B1).
- 287 Antolik, M., Dreger, D., & Romanowicz, B. (1996). Finite fault source study of the
 288 great 1994 deep Bolivia earthquake. *Geophysical research letters*, *23*(13), 1589–
 289 1592.
- 290 Bina, C. R. (1997). Patterns of deep seismicity reflect buoyancy stresses due to
 291 phase transitions. *Geophysical research letters*, *24*(24), 3301–3304.

- 292 Boatwright, J. (1980). A spectral theory for circular seismic sources; simple esti-
 293 mates of source dimension, dynamic stress drop, and radiated seismic energy.
 294 *Bulletin of the Seismological Society of America*, *70*(1), 1–27.
- 295 Branch, M. A., Coleman, T. F., & Li, Y. (1999). A subspace, interior, and conjugate
 296 gradient method for large-scale bound-constrained minimization problems.
 297 *SIAM Journal on Scientific Computing*, *21*(1), 1–23.
- 298 Brune, J. N. (1970). Tectonic stress and the spectra of seismic shear waves from
 299 earthquakes. *Journal of geophysical research*, *75*(26), 4997–5009.
- 300 Calderoni, G., Rovelli, A., Ben-Zion, Y., & Di Giovambattista, R. (2015). Along-
 301 strike rupture directivity of earthquakes of the 2009 L’Aquila, central italy,
 302 seismic sequence. *Geophysical Journal International*, *203*(1), 399–415.
- 303 Campus, P., & Das, S. (2000). Comparison of the rupture and radiation character-
 304 istics of intermediate and deep earthquakes. *Journal of Geophysical Research:
 305 Solid Earth*, *105*(B3), 6177–6189.
- 306 Chen, Y., & Wen, L. (2015). Global large deep-focus earthquakes: Source process
 307 and cascading failure of shear instability as a unified physical mechanism.
 308 *Earth and Planetary Science Letters*, *423*, 134–144.
- 309 Dziewonski, A. M., & Anderson, D. L. (1981). Preliminary reference Earth model.
 310 *Physics of the earth and planetary interiors*, *25*(4), 297–356.
- 311 Eshelby, J. D. (1957). The determination of the elastic field of an ellipsoidal inclu-
 312 sion, and related problems. *Proceedings of the Royal Society of London. Series
 313 A. Mathematical and Physical Sciences*, *241*(1226), 376–396.
- 314 Fan, W., Wei, S. S., Tian, D., McGuire, J. J., & Wiens, D. A. (2019). Complex and
 315 Diverse Rupture Processes of the 2018 Mw 8.2 and Mw 7.9 Tonga-Fiji Deep
 316 Earthquakes. *Geophysical Research Letters*, *46*(5), 2434–2448.
- 317 Frankel, A., & Wennerberg, L. (1989). Microearthquake spectra from the Anza, Cal-
 318 ifornia, seismic network: site response and source scaling. *Bulletin of the Seis-
 319 mological Society of America*, *79*(3), 581–609.
- 320 Frohlich, C. (1989). The nature of deep-focus earthquakes. *Annual Review of Earth
 321 and Planetary Sciences*, *17*(1), 227–254.
- 322 Goto, K., Suzuki, Z., & Hamaguchi, H. (1987). Stress distribution due to olivine-
 323 spinel phase transition in descending plate and deep focus earthquakes. *Jour-
 324 nal of Geophysical Research: Solid Earth*, *92*(B13), 13811–13820.
- 325 Green, H., & Burnley, P. (1989). A new self-organizing mechanism for deep-focus
 326 earthquakes. *Nature*, *341*(6244), 733.
- 327 Green, H., Shi, F., Bozhilov, K., Xia, G., & Reches, Z. (2015). Phase transformation
 328 and nanometric flow cause extreme weakening during fault slip. *Nature Geo-
 329 science*, *8*(6), 484.
- 330 Green, H. W., & Houston, H. (1995). The mechanics of deep earthquakes. *Annual
 331 Review of Earth and Planetary Sciences*, *23*(1), 169–213.
- 332 Houston, H. (2015). 4.13 - Deep Earthquakes. In G. Schubert (Ed.), *Treatise on geo-
 333 physics (second edition)* (Second Edition ed., p. 329 - 354). Oxford: Elsevier.
 334 doi: <https://doi.org/10.1016/B978-0-444-53802-4.00079-8>
- 335 Huang, Y., Beroza, G. C., & Ellsworth, W. L. (2016). Stress drop estimates of po-
 336 tentially induced earthquakes in the Guy-Greenbrier sequence. *Journal of Geo-
 337 physical Research: Solid Earth*, *121*(9), 6597–6607.
- 338 Imanishi, K., & Ellsworth, W. L. (2006). Source scaling relationships of mi-
 339 croearthquakes at Parkfield, CA, determined using the SAFOD pilot hole
 340 seismic array. *Earthquakes: Radiated Energy and the Physics of Faulting*, *170*,
 341 81–90.
- 342 Kanamori, H., & Anderson, D. L. (1975). Theoretical basis of some empirical re-
 343 lations in seismology. *Bulletin of the seismological society of America*, *65*(5),
 344 1073–1095.
- 345 Kanamori, H., Anderson, D. L., & Heaton, T. H. (1998). Frictional melting during
 346 the rupture of the 1994 Bolivian earthquake. *Science*, *279*(5352), 839–842.

- 347 Kanamori, H., & Brodsky, E. E. (2004). The physics of earthquakes. *Reports on*
 348 *Progress in Physics*, *67*(8), 1429.
- 349 Kaneko, Y., & Shearer, P. (2014). Seismic source spectra and estimated stress drop
 350 derived from cohesive-zone models of circular subshear rupture. *Geophysical*
 351 *Journal International*, *197*(2), 1002–1015.
- 352 Karato, S.-i., Riedel, M. R., & Yuen, D. A. (2001). Rheological structure and de-
 353 formation of subducted slabs in the mantle transition zone: implications for
 354 mantle circulation and deep earthquakes. *Physics of the Earth and Planetary*
 355 *Interiors*, *127*(1-4), 83–108.
- 356 Kikuchi, M., & Kanamori, H. (1994). The mechanism of the Deep Bolivia Earth-
 357 quake of June 9, 1994. *Geophysical Research Letters*, *21*(22), 2341–2344. doi:
 358 10.1029/94GL02483
- 359 Kirby, S. H. (1987). Localized polymorphic phase transformations in high-pressure
 360 faults and applications to the physical mechanism of deep earthquakes. *Journal*
 361 *of Geophysical Research: Solid Earth*, *92*(B13), 13789–13800.
- 362 Madariaga, R. (1976). Dynamics of an expanding circular fault. *Bulletin of the Seis-*
 363 *mological Society of America*, *66*(3), 639–666.
- 364 Meng, L., Ampuero, J.-P., & Bürgmann, R. (2014). The 2013 Okhotsk deep-focus
 365 earthquake: Rupture beyond the metastable olivine wedge and thermally con-
 366 trolled rise time near the edge of a slab. *Geophysical Research Letters*, *41*(11),
 367 3779–3785.
- 368 Mueller, C. S. (1985). Source pulse enhancement by deconvolution of an empirical
 369 Green’s function. *Geophysical Research Letters*, *12*(1), 33–36.
- 370 Paola, N. D., Holdsworth, R. E., Viti, C., Collettini, C., & Bullock, R. (2015).
 371 Can grain size sensitive flow lubricate faults during the initial stages of earth-
 372 quake propagation? *Earth and Planetary Science Letters*, *431*, 48 - 58. doi:
 373 <https://doi.org/10.1016/j.epsl.2015.09.002>
- 374 Persh, S. E., & Houston, H. (2004). Strongly depth-dependent aftershock production
 375 in deep earthquakes. *Bulletin of the Seismological Society of America*, *94*(5),
 376 1808–1816.
- 377 Poli, P., & Prieto, G. (2014). Global and along-strike variations of source dura-
 378 tion and scaling for intermediate-depth and deep-focus earthquakes. *Geophys-*
 379 *ical Research Letters*, *41*(23), 8315–8324.
- 380 Poli, P., & Prieto, G. A. (2016). Global rupture parameters for deep and
 381 intermediate-depth earthquakes. *Journal of Geophysical Research: Solid Earth*,
 382 *121*(12), 8871–8887.
- 383 Ross, Z. E., & Ben-Zion, Y. (2016). Toward reliable automated estimates of earth-
 384 quake source properties from body wave spectra. *Journal of Geophysical Re-*
 385 *search: Solid Earth*, *121*(6), 4390–4407.
- 386 Ruhl, C., Abercrombie, R., & Smith, K. (2017). Spatiotemporal variation of stress
 387 drop during the 2008 Mogul, Nevada, earthquake swarm. *Journal of Geophys-*
 388 *ical Research: Solid Earth*, *122*(10), 8163–8180.
- 389 Sato, T., & Hirasawa, T. (1973). Body wave spectra from propagating shear cracks.
 390 *Journal of Physics of the Earth*, *21*(4), 415–431.
- 391 Shearer, P. M., Abercrombie, R. E., Trugman, D. T., & Wang, W. (2019). Compar-
 392 ing EGF methods for estimating corner frequency and stress drop from P wave
 393 spectra. *Journal of Geophysical Research: Solid Earth*.
- 394 Shearer, P. M., Prieto, G. A., & Hauksson, E. (2006). Comprehensive analysis of
 395 earthquake source spectra in southern California. *Journal of Geophysical Re-*
 396 *search: Solid Earth*, *111*(B6).
- 397 Tingle, T. N., Green, H. W., Scholz, C. H., & Koczyński, T. (1993). The rheology
 398 of faults triggered by the olivine-spinel transformation in Mg₂GeO₄ and its im-
 399 plications for the mechanism of deep-focus earthquakes. *Journal of Structural*
 400 *Geology*, *15*(9-10), 1249–1256.
- 401 Vallée, M. (2013). Source time function properties indicate a strain drop indepen-

- 402 dent of earthquake depth and magnitude. *Nature communications*, *4*, 2606.
- 403 Ye, L., Lay, T., Kanamori, H., & Koper, K. D. (2013). Energy release of the 2013
404 Mw 8.3 Sea of Okhotsk earthquake and deep slab stress heterogeneity. *Science*,
405 *341*(6152), 1380–1384.
- 406 Yoshioka, S., Daessler, R., & Yuen, D. A. (1997). Stress fields associated with
407 metastable phase transitions in descending slabs and deep-focus earthquakes.
408 *Physics of the earth and planetary interiors*, *104*(4), 345–361.
- 409 Zhan, Z. (2017). Gutenberg–Richter law for deep earthquakes revisited: A dual-
410 mechanism hypothesis. *Earth and Planetary Science Letters*, *461*, 1–7.
- 411 Zhan, Z., Kanamori, H., Tsai, V. C., Helmberger, D. V., & Wei, S. (2014).
412 Rupture complexity of the 1994 Bolivia and 2013 Sea of Okhotsk deep
413 earthquakes. *Earth and Planetary Science Letters*, *385*, 89 - 96. doi:
414 <https://doi.org/10.1016/j.epsl.2013.10.028>
- 415 Zhan, Z., Shearer, P. M., & Kanamori, H. (2015). Supershear rupture in the 24
416 May 2013 Mw 6.7 Okhotsk deep earthquake: Additional evidence from regional
417 seismic stations. *Geophysical Research Letters*, *42*(19), 7941–7948.